Carbohydrate Polymers 84 (2011) 126–132

Contents lists available at ScienceDirect

Carbohydrate Polymers

journal homepage: www.elsevier.com/locate/carbpol

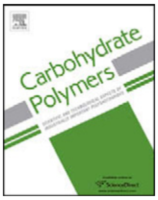

Self-assembled polystyrene/xyloglucan nanospheres from spin coating evaporating mixtures

Adriana F. Lubambo[a,b,*], Neoli Lucyszyn[b], Cesar L. Petzhold[c], Paulo C. de Camargo[a], Maria-R. Sierakowski[b], Wido H. Schreiner[a], Cyro K. Saul[a]

[a] Department of Physics, Universidade Federal do Paraná-UFPR, Centro Politécnico, P.O Box 19044, Curitiba, Brazil
[b] Department of Chemistry, Biopol, Universidade Federal do Paraná-UFPR, Centro Politécnico, P.O. Box 19081, Curitba, Brazil
[c] Department of Organic Chemistry, Universidade Federal do Rio Grande do Sul- UFRGS, Campus do Vale, P.O Box 15003, Porto Alegre, Brazil

ARTICLE INFO

Article history:
Received 16 September 2010
Accepted 4 November 2010
Available online 12 November 2010

Keywords:
Organic thin films
Mixtures
Self-assembly
Nanosphere arrays
Spin coating
Xyloglucan
Polystyrene

ABSTRACT

Thin polystyrene–polysaccharide films were deposited on mica by spin coating evaporating mixtures. Solutions of PS (polystyrene) in chloroform (15, 30 and 60 mg/L) and XG (xyloglucan) in water (15 mg/L) were prepared and mixed by stirring in different proportions. After evaporation by spin coating, a low order array of nanospheres was observed by AFM on top of a homogeneous layer, contingent on the proportion of the components in the original mixtures. A XG nanosphere array formed on top of a polystyrene layer was obtained from mixtures containing from 5 to 30% (v/v) of a 15 mg/L XG solution and 95–70% (v/v) of a 15 mg/L PS solution. XPS results showed that equal amounts of XG and PS were adsorbed on the mica substrate for 50% (v/v) XG as well as for 10% (v/v) XG mixtures. PS adsorption was not detected when the XG proportion was 90% (v/v). PS nanospheres were only obtained on top of the XG layer when the PS concentration was increased to four times the original solution. Furthermore, for a constant spin coating speed, the nanosphere diameter was found to be independent of the component proportion within the investigated range. We also found that the nanosphere diameter is correlated to the inverse square-root of the spin coating speed.

1. Introduction

Nanoscale patterned thin films are of fundamental importance for several applications, especially when the resulting pattern is driven by self-assembly. Among their many advantages are the ease and speed of bottom-up production methods as compared with top-down techniques, where nanoscale features must be fabricated in several complex and time-consuming steps. Usually, those steps rely on sophisticated equipment and materials (Del Campo & Artz, 2008; Powell, Tran, Kim, & Yoon, 2009; Tormen et al., 2004). Furthermore, if the physico-chemical character of the resulting pattern can be modified by simply changing concentrations, it would have the advantage of flexibility on demand. Mixing materials of both natural and synthetic origin, as in bioblends, may lead to further improvement in their mechanical and/or chemical properties (Biresaw, Carriere, & Willett, 2004). In the case that one of the components is of natural, renewable origin, the final product would be more "green." One class of such green materials are neutral polysaccharides, which have already been used in solid-phase diagnostics to avoid non-specific protein adsorption (Malmsten, 2003).

One of the many routes to producing bioblends is the emulsification process, which is well known and applied in various fields including: cosmetics; the food industry; coatings; lubricants and pharmaceuticals (Tadros, 2009). More recently, conventional emulsions were used to produce nanoparticles (Desgouilles et al., 2003), high-internal-phase emulsions (HIPE) to obtain organic semiconducting polymer blends (Mezzenga et al., 2003) and microemulsions to permit manufacture of well-defined pore morphology particles (Carroll, Pylypenko, Atanassov, & Petsev, 2009). In all of these studies, evaporation played an important role. The drying process, in particular the rate and the mechanism behind solvent evaporation, has a large impact on the resulting morphology.

One low cost and easy way of preparing such bottom-up nanostructures is the spin coating technique. Spin coating is a complex non-equilibrium process whose behavior can be explained by several different models, chosen according to the underlying assumptions and approximations (Acrivos, Shah, & Peterson, 1960; Bornside, Macosko, & Scriven, 1987; Emslie, Bonner, & Peck, 1958; Lawrence, 1988; Meyerhofer, 1978; Norrman, Ghanbari-Siahkali, & Larsen, 2005; Zhao & Marshall, 2008). Regardless of the applied model, this well-known technique allows 2D structuring of parti-

---

[*] Corresponding author at: UFPR, Av. Cél. Francisco H. dos Santos, Centro Politécnico, Jardim das Américas, 81531-990, Curitiba, PR, Brazil. Tel.: +55 41 33613092; fax: +55 41 33613418.

E-mail addresses: af.lubambo@uol.com.br, af.lubambo@gmail.com (A.F. Lubambo).

0144-8617/$ – see front matter © 2010 Elsevier Ltd. All rights reserved.
doi:10.1016/j.carbpol.2010.11.010

cles whose morphology depends on the manufacturing conditions (Hulteen & van Duyne, 1995; Liu, Chang, Ko, Chu, & Daí, 2003). Nonetheless, the literature on spin coated thin films is mostly related to polymer and small particle suspensions, with diameters ranging from 100 nm to 5 μm (Zhao & Marshall, 2008). To the best of our knowledge, there are only a few reports on the study of liquid phase emulsion drying (Aranberri, Beverley, Binks, Clint, & Fletcher, 2002; Clint, Fletcher, & Todorov, 1999; Friberg & Langlois, 1992; Langlois & Friberg, 1993; Leal-Calderon, Mondain-Monval, Pays, Royer, & Bibette, 1997), and even fewer on droplet emulsion evaporation (Auguste & Levy, 2009; Kapilashrami, Eskilsson, Bergström, & Malmsten, 2004) and none related to mixture drying under centrifugal and shear-forces.

We are interested in the study of spin coated self-assembled thin films, starting with xyloglucan–polystyrene mixtures, and its potential application in solid-phase diagnostics. Xyloglucan is a neutral, branched polysaccharide found in the primary cell walls of non-graminaceous (monocotyledons) seeds, as well as in the cotyledon of some dicotyledonous seeds. In addition to its structural function, it also acts as energy storage (Fry, 1989; Hayashi, 1989; Reid, 1985). Its chemical structure has a cellulose-like backbone, composed of β-glucosyl ring units with ribbon-like conformation, where single units of xylose and galactose substituents form a part of the branches (Hayashi, 1989). This biopolymer, like many other polysaccharides, is potentially important for commercial and medical applications. In the food industry, it can be used as a texture modifier, and in medical applications, it can act as a drug release controller (Bhattacharya, Bal, Mukherjee, & Bhattacharya, 1991; Miyazaki et al., 1998; Miyazaki, Kawasaki, Kubo, Endo, & Attwood, 2001).

Polystyrene thin films are, by far, the most studied polymer system (Forrest, 2002). Because it is a non-biodegradable polymer, when it is used conjunction with degradable one, it reduces the degradation rate and can therefore be used in tissue engineering and drug release control (Leung et al., 2009).

2. Materials and methods

2.1. Polysaccharide

Branched neutral polysaccharide xyloglucan (XG) (M_w of 843,000 g/mol) was extracted from the seeds of *Guibourtia hymenifolia*. The XG (yield 54%, w/w) was formed in a glucose:xylose:galactose ratio of 3.3:2.3:1. After extraction, the XG was purified with a 0.22 μm millipore filter before use.

2.2. Polystyrene

The polystyrene (PS) (M_w of 52,700 g/mol; $M_w/M_n = 1.1$) used in this investigation was prepared by ATRP polymerization. Styrene (freshly distilled) was polymerized in bulk at 60 °C using 2-bromethyl isobutyrate as an initiator and CuBr/PMDETA (N,N′,N′,N″,N″-pentamethyldiethylenetriamine) as a catalyst in a molar ratio of 500:1:1:1. After 20 h, the reaction was quenched and the polymer precipitated in ethanol and dried under vacuum. All reagents were purchased from Aldrich Polymer. The molecular weight was determined in a GPCmax Viscotek Triple-detector equipment using a PS calibration curve and THF (1 mL/min) as eluent.

2.3. Substrate

A grade V-4 mica muscovite substrate obtained from SPI Supplies® was tape cleaved and immediately used for the adsorption experiments.

2.4. Adsorption protocols for model surfaces

Xyloglucan solution was prepared with 1.5 mg of XG dissolved in 100 mL of milli-Q water and stirred for 24 h. Polystyrene solutions were prepared at three different concentrations with 1.5, 3.0 and 6.0 mg of PS in 100 mL chloroform. The mixtures were prepared by mixing different proportions (1 mL final volume) of XG with PS solutions.

The mixtures were prepared by stirring the solutions for 1 min in a vortex prior to spin coat deposition. A drop (20 μL) of mixture was immediately pipetted onto the center of a mica substrate that was rotating at 1000 rpm and kept at the same conditions for 1 min. The substrate was then accelerated to 2000 rpm and maintained at this speed for 30 s. The sample was not rinsed during spinning. After deposition, the samples were kept in a controlled chamber at 24 °C and 45% relative humidity for 24 h before they were ready for analysis.

2.5. Atomic force microscopy measurements

AFM imaging was performed using a commercial Shimadzu SPM-9500J3 microscope at room temperature (~24 °C). Images were taken in dynamic tapping mode (TM-AFM) with an oxide-sharpened micro-fabricated silicon cantilever (μ-Masch) whose nominal spring constant was 4.7 N/m and whose tip radius of curvature was less than 10 nm. The scanning rate was 1 Hz and the image resolution was 256 × 256 pixels. The operating point was adjusted to minimize the interaction between the tip and the sample in order to avoid soft layer deformation. After acquisition, image treatment was performed using Shimadzu software for flattening. Grain analysis was performed using threshold detection and histograms were carried out using SPIP V.4.3.4.0. The image background was noise filtered whenever needed prior to contour detection. Fourier analysis was performed using Image J (1.42q, NIH) software. The images were first transformed into binary mode to eliminate any scan noise left and then a Fast Fourier Transform (FFT) was applied to access information about orientation and texture.

2.6. X-ray photoelectron spectroscopy measurements

XPS analyses were performed with an ESCA 3000 VG Microtech photoelectron spectrometer. Aluminum K_α radiation was used and high resolution spectra were taken with 20 eV pass energy. The vacuum in the sample chamber during measurements was about 10^{-9} mbar. Charging effects were corrected using the Si 2p line (102.7 eV) for mica as a reference (Bhattacharyya, 1989; Dufrêne, Marchal, & Rouxhet, 1999; Liu & Brown, 1998). Data treatment was carried out using XI_SDP32V.3 from XPS International© software. Element concentrations were evaluated from peak areas after Shirley background subtraction.

2.7. Scanning electron microscopy

SEM analysis was performed on a JEOL Model JSM6360LV using secondary electrons at 15 kV with a 13 mm working distance and a spot size of 49 (about 10 nm) to increase contrast. The samples were prepared by sputter coating with gold.

3. Results and discussion

3.1. XG (15 mg/L) and PS (15 mg/L)

3.1.1. Morphological analysis

Dynamic mode AFM images of XG/PS thin films on mica show different morphologies as a function of XG/PS proportions in the mixture, as shown in Fig. 1. At XG proportions from 5% to about 30%

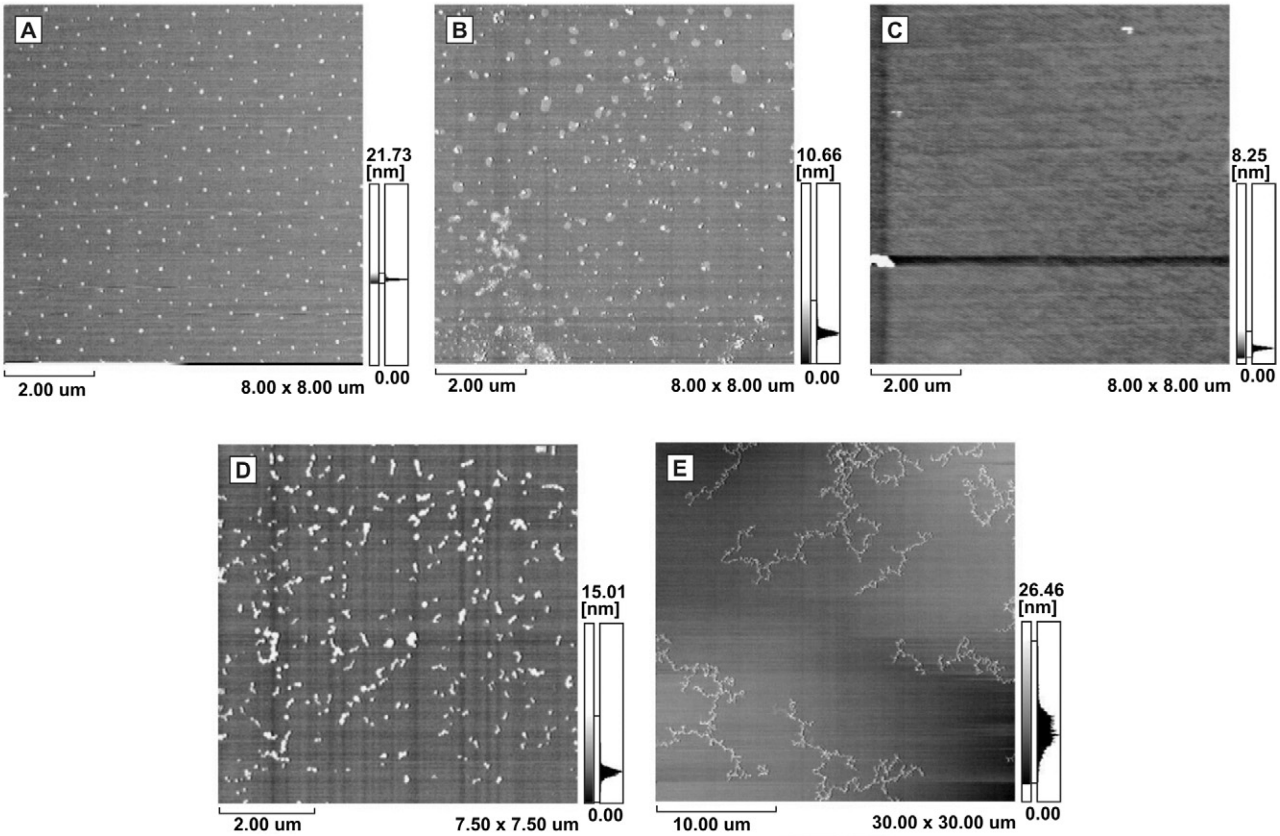

Fig. 1. Dynamic mode AFM images. (A) XG/PS (10/90%) sample showing XG nanospheres on a PS matrix (8 μm × 8 μm). (B) XG/PS (50/50%) sample (8 μm × 8 μm). (C) XG/PS (90/10%) sample (8 μm × 8 μm). (D) 100% PS sample, PS_c = 15 mg/L (7.5 μm × 7.5 μm). (E) 100% XG sample, XG_c = 15 mg/L (30 μm × 30 μm).

XG, nanosphere arrays on top of a homogeneous background layer were observed, as seen in Fig. 1A for 10% XG. For higher XG proportions, i.e., XG/PS (50/50%), as shown in Fig. 1B, the assembly and the structure of the nanosphere array becomes non-reproducible. Finally, a nanosphere array was not observed for XG/PS (90/10%) under any circumstances, as shown in Fig. 1C. It is worth remarking that for pure XG aqueous solution and pure PS chloroform solution, shown in Fig. 1D and E, respectively, the thin films present completely different morphologies compared with the mixed solutions. Pure PS can form irregular, non-correlated, granular aggregates, and pure XG produces Brownian aggregates (Julien & Botet, 1987) with fractal dimension equal to 1.38, as calculated by the Image J program.

Mixtures with XG concentrations ranging from 5% to about 30% present arrays with short-range order, as evidenced by the regular features and repeating distances shown in Figs. 1A and 2A for the XG/PS (10/90%) sample. Fig. 2B shows the FFT of Image 2A, which confirms the existence of characteristic length-scales and whose radially symmetric transform image indicates the isotropy of this arrangement (Russ, 1998). The first wavelength, which is related to the diameter of the circle in reciprocal space, corresponds to 46 pixels. This feature indicates objects of about 87 nm in diameter in real space because each pixel of the image in reciprocal space corresponds to $2.5 \times 10^{-4}\,\text{nm}^{-1}$. Grain analysis for the minimum diameter of the sphere is 78 nm, as shown in Table 1. Thus, the observed result is within the range determined by grain analysis and is in good agreement with the FFT analysis.

Other characteristic wavelengths can be determined through profiles taken at 0° (coordinate axis in the center of figure) in the FFT, indicating periodic features of about 330 nm, as seen in Fig. 2A.

It is known that spin coating allows the formation of organized patterns under certain conditions. The final pattern is a result of a complex mechanism that comprises the existence of three stages: solution dispensing, balance between viscous and centrifugal forces and fluid evaporation (Lawrence, 1988). Under certain conditions, a combination of the second and the third stages can lead to low-ordered arrangements (Kralchevsky & Denkov, 2001).

We focus our attention on the two final stages to explain the resulting nanosphere pattern seen in Fig. 1A. After the mixture is dispensed, there will be a concentration gradient of water/XG droplets (dispersed phase) in the chloroform/PS continuum phase which is perpendicular to the substrate surface. The possible mechanisms responsible for such a gradient are well known (Tadros, 2009). Another important mechanism which may induce a concentration gradient is the thinning of the continuum phase during the second and third stages due to centrifugal forces and solvent evaporation, respectively.

As the second stage starts, the continuum phase is pushed outwards by centrifugal forces and the droplets are carried outward by viscosity forces as well as by centrifugal force. In the case of water/XG droplets, a perpendicular diffusion process drives them toward the air–liquid interface. As the continuum phase thins and approaches the size of the droplets, both frictional forces at the substrate interface and lateral capillary forces start to become appreciable, keeping the droplets at an equilibrium distance, inducing self-assembly (Kralchevsky & Denkov, 2001). In fact, the lateral capillary force acts on partially immersed or confined droplets lying across the gas–liquid interface. The lateral forces pull the droplets toward each other, maintaining them at a characteristic distance, reducing their perturbation on the liquid surface, thus promoting self-assembly. The final film thickness measured by scraping the surface of the XG/PS (25/75%) sample with the AFM tip was about 3 nm, strongly supporting our hypothesis.

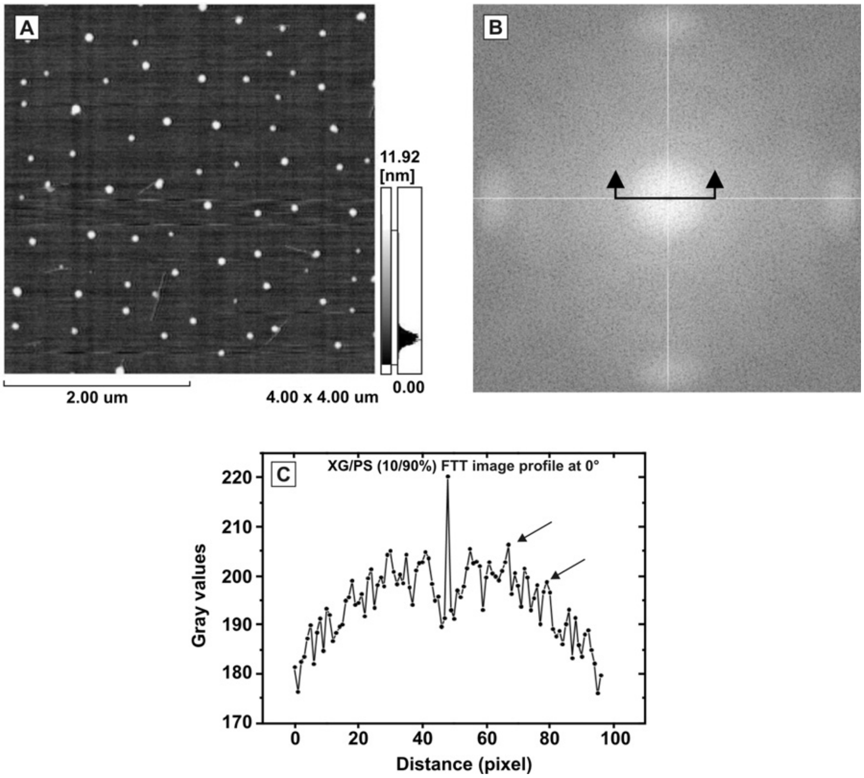

Fig. 2. (A) Dynamic mode AFM image of the XG/PS (10/90%) sample (4 μm × 4 μm). (B) Fourier transform of image (A). (C) Corresponding FFT gray profile at $\theta = 0^{\circ}$.

When the continuum phase thickness reaches a minimum, the droplets will remain at the same position until the entire continuum phase is evaporated. In these conditions XG/PS (10/90%) in which the continuum phase is chloroform/PS, thinning occurs more quickly compared with a water based continuum phase due to both low viscosity and high volatility. Therefore, the droplets will reach their resting positions more quickly than when the continuum phase is water based, and the effects of the diffusion mechanisms perpendicular to the substrate can be considered as negligible. Such conditions favor the self-assembly of XG nanospheres on the surface.

Measured average diameters D as a function of XG and PS mixture proportions are presented in Table 1. However, these diameters are overestimated due to the tip convolution effect. Taking this into account, the final diameters D^* were calculated using (Engel, Schoenenberger, & Müller, 1997).

$$D = \sqrt[2]{RD^* + \frac{D^{*2}}{4}} \qquad (1)$$

with the assumption that the AFM tip is spherical with radius of curvature $R = 10$ nm.

As seen in Table 1, fluctuations in the diameter D do not suggest any significant correlation between D and the proportions of the mixture components.

In the complementary mixture series, water/XG becomes the continuum phase and chloroform/PS forms droplets, as the dispersed phase. Fig. 1C shows that no nanosphere patterns are seen for the XG/PS (90/10%) samples, as the denser chloroform/PS droplets will tend to diffuse toward the substrate. When centrifugal forces start to drag the continuous phase, the higher viscosity of water will help to drive chloroform/PS droplets outwards. Because the vapor pressure of water is almost one order of magnitude less than that of chloroform, its volatility is significantly smaller. Thus, thinning of the continuous layer will be dominated by outward flow instead of by evaporation, and the probability that the PS nanospheres will be washed away increases significantly. SEM images show that while a few chloroform/PS droplets may remain on the substrate, they are buried and entangled within the remaining XG layer, and therefore would not be observed.

Fig. 3 shows a plot of the measured average diameter as a function of spinning speed. In the range from 400 rpm to 1100 rpm, the average diameter depends on the inverse of the square-root of the spinning speed (SS) and scales as the inverse of evaporation rate (Birnie & Manley, 1997) with a correlation coefficient of 0.995.

3.1.2. *Chemical analysis*

Mica is a known hydrous aluminosilicate $KAl_2Si_3AlO_{10}(OH)_2$ whose structure is composed of three layers; the outer two are tetrahedral and the interstitial layer is mostly comprised of octahedrally arranged aluminum atoms. The tetrahedral layers are

Table 1
Average diameter D and standard deviation (δD) of the measured nanospheres as a function of XG and PS proportion in mixture, as well as its tip deconvolved D^* correspondents.

Parameter	XG/PS proportion (%)					
	(5/95)	(10/90)	(15/85)	(20/80)	(25/75)	(30/70)
$D \pm \delta D$ (nm)	101 ± 13	95 ± 17	93 ± 11	103 ± 12	99 ± 20	91 ± 24
D^* (nm)	83	77	75	85	81	73

Measured diameter: D (nm) and standard deviation: δD (nm), deconvolved tip diameter: D^* (nm).

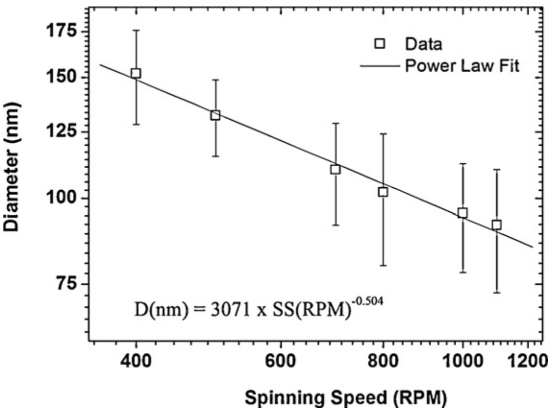

Fig. 3. Measured average diameter as a function of spinning speed (SS), XG/PS (10/90%) sample.

Table 2
Relative elemental surface composition (at.%) detected by XPS analysis of the samples adsorbed on the mica surface. The quantities C/Si and O/Si normalize the peak area ratio.

Sample	Na%	K%	Al%	O%	C%	Si%	O/Si	C/Si
Bare mica	1.5	3.4	16.8	54.3	3.5	20.5	2.6	0.17
XG/PS (90/10%)	0.4	3.7	10.4	49.2	18.8	17.7	2.8	1.06
XG/PS (50/50%)	2.5	3.6	8.4	41.6	28.7	15.1	2.8	1.9
XG/PS (10/90%)	0.4	3.1	9.6	43.2	28.2	15.4	2.8	1.83
XG/PS (10/90%) washed	0.8	3.8	12.7	52.5	9.9	20.3	2.6	0.48
100% PS	0.9	4.8	12.7	51.3	10.9	19.4	2.6	0.56
100% XG	0.5	4.0	12.0	51.6	13.0	18.8	2.7	0.7

negatively charged because one-fourth of the tetravalent silicon atoms are substituted by trivalent aluminum ones. This creates a negative charge that is balanced by potassium ions or impurities such as sodium, which can also substitute for aluminum (Battacharryya, 1993).

The XPS spectrum of bare mica substrate shown in Table 2 indicates the presence of 3.5% elemental carbon. This small amount of carbon is due to impurities and is always present in ambient conditions (C 1s, Eb = 284.4–285.6 eV). Both carbon and oxygen percentages in each sample were normalized to bulk silicon to allow a comparison between different samples. Bulk silicon was chosen because of its well-defined stoichiometric composition in the mica substrate.

We found that the Al 2p/Si 2p ratio is 0.82 for the mica substrate, which is close to the calculated ratio of 0.87 for bulk mica (Battacharryya, 1993). The reason for such small discrepancies in the Al 2p/Si 2p ratio for all other samples could be due to the attenuation of photoelectrons originating from the octahedral layer when they cross the carbon thin film layer. Another reason may be the low sensitivity of XPS to aluminum (Battacharryya, 1993).

The K 2p/Si 2p ratio for all samples was found to be 0.2, which is very close to the elemental ratio obtained. When corrected for 37% attenuation, this calculated value is 0.3. For this correction, it was considered that the photoelectron mean free path for insulating and semi-conducting oxides is 13 Å (Cox, Egdell, Harding, Patterson, & Tavener, 1982), while they originate from a depth of 10 Å, which is the distance between cleavage planes. Therefore, the data in Table 2 can be taken as fairly representative of the relative elemental sample surface composition.

The oxygen (O/Si = 2.6) detected in the 100% PS sample can be attributed to the mica substrate. Based on the tabulated data, most of the presence of oxygen in the remaining samples can be attributed to the mica substrate while there is only a small contribution from XG ($XG_{O/Si} = 0.1$). Furthermore, the carbon present in the XG sample, excluding impurities (0.17 – which is an approximate value taken, for example, from bare mica), is found to be $XG_{C/Si} = 0.53$. For 100% PS, the carbon present is $PS_{C/Si} = 0.39$.

The 90% XG sample yields O/Si = 2.8. Assuming that O/Si = 2.6 can be attributed to the mica substrate, the excess oxygen ($XG_{O/Si} = 0.2$) must be linked with the XG content, which indicates twice as much oxygen as in 100% XG. Another issue relevant to this matter relates to the high carbon ratio in this sample ($XG_{C/Si} = 1.06$) when compared with pure XG. Using simple algebra, if we consider the pure XG ratio ($XG_{C/Si} = 0.7$), discount the carbon impurity value taken from the bare mica measurement, and multiply this result by 2, based on the oxygen increase the result is exactly the XG ratio of the 90% XG sample ($XG_{C/Si} = 1.06$). This good agreement is confirmed by the fact that we did not observe polystyrene nanospheres on the sample, as shown in Fig. 1C. One possible explanation for such behavior is related to the hydrophilic character of both mica and XG, which makes them more compatible than PS and mica. The small amount of PS in the mixture also plays a role in the final result.

In the 50% XG sample, the carbon ratio from XG, excluding impurities, would be roughly equal to $XG_{C/Si} = 0.53 \times 2 = 1.06$, as in the previous sample. The remaining carbon ratio is from polystyrene and is expected to be $PS_{C/Si} = 0.39 \times 2 = 0.78$, leading to a total carbon ratio in the sample of $PS_{C/Si} = 1.84$. The measured ratio is of $PS_{C/Si} = 1.9$ which is in good agreement with this analysis.

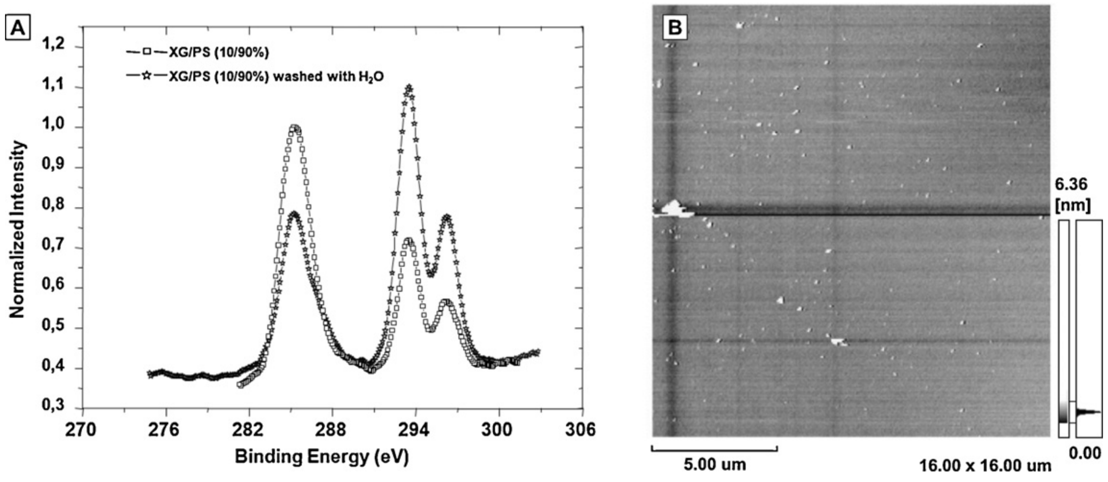

Fig. 4. (A) XPS C 1s and K $2p_{3/2}$ and K $2p_{1/2}$ spectra of the XG/PS (10/90%) sample and the same sample after selective dissolution with water. (B) AFM image of the XG/PS (10/90%) sample after selective dissolution with water (16 μm × 16 μm).

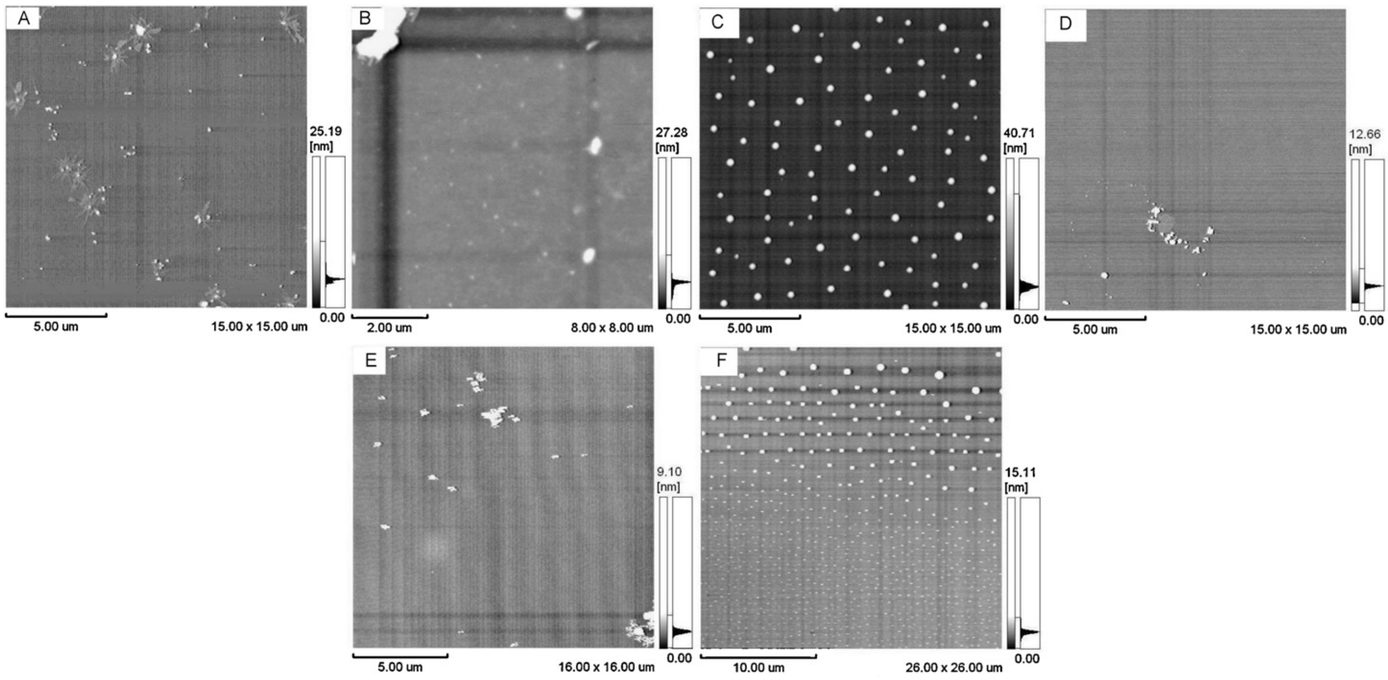

Fig. 5. Dynamic mode AFM images for $XG_c = 15$ mg/L, $PS_c = 30$ mg/L, original solution concentrations, indicating an absence of a nanosphere pattern for high XG percentage samples: (A) the XG/PS (80/20%) sample (15 μm × 15 μm) and (B) the XG/PS (70/30%) sample (8 μm × 8 μm). Dynamic mode AFM for $XG_c = 15$ mg/L, $PS_c = 60$ mg/L, original solution concentrations. (C) XG/PS (70/30%) sample (15 μm × 15 μm). (D) The previous sample (C) after selective dissolution with chloroform (15 μm × 15 μm). (E) XG/PS (80/20%) sample deposited at 2000 rpm (16 μm × 16 μm). (F) Sample with same constituent proportions as in (E), deposited at 1000 rpm (26 μm × 26 μm).

The 10% XG sample follows the same behavior as the 50% XG sample and presents equal adsorbed amounts of both XG and PS. The composition of the nanospheres shown in Fig. 1A was tested by selectively washing the sample five times with 1 mL of milli-Q water. After washing, the disappearance of the assembled pattern of nanospheres was observed, as was the presence of a few remaining aggregates, as shown in Fig. 4B.

The decrease in intensity of the C 1s peak in the XPS spectrum, shown in Fig. 4A, indicates material removal. The results in Table 2 show that the remaining oxygen (O/Si = 2.6) and carbon (C/Si = 0.48) ratios are almost the same as for pure PS. This result suggests that the nanospheres are composed of XG, which was withdrawn by washing, and the remaining bottom layer is composed of polystyrene.

3.2. XG (15 mg/L) and PS (30 mg/L)

Based on the results of the previous section, we have increased the PS concentration in the original solutions, and therefore in the final mixtures, to force the appearance of PS nanospheres on top of a homogenous XG layer.

3.2.1. Morphological analysis

Although we doubled the concentration of PS in the initial solution, and therefore in the final high water/XG proportion mixtures (between 70% and 95%), we were not able to observe PS nanosphere patterns, as shown in Fig. 5A and B. Instead, either star-shape aggregates on top of an homogeneous layer were observed, as seen in Fig. 5A for the XG/PS (80/20%) sample, or just aggregates, as depicted in Fig. 5B for the XG/PS (70/30%) sample.

We speculate that this is due to the average dimension of the chloroform/PS droplets and the final PS nanosphere average diameter. The nanospheres are apparently still small enough to be completely washed away, while the remaining nanospheres are buried below the XG layer.

3.3. XG (15 mg/L) and PS (60 mg/L)

To further ensure the appearance of PS nanospheres on the samples, the PS concentration was again doubled.

3.3.1. Morphological analysis

Within the mixture proportion range tested, from 5% to 30% PS, as shown in Fig. 5C for the XG/PS (70/30%) sample, the only sample which did not present nanosphere patterns was the 5% PS mixture. This means that we achieved the level where the particles' average size is sufficient to ensure their anchoring to the substrate while the continuous layer is thinning during the second phase of the spinning process. Confirmation that the nanospheres are composed of PS was obtained by selectively washing the surface with 20 μL of chloroform. The nanosphere array was completely removed, leaving a homogenous layer with a few aggregates, as shown in Fig. 5D.

SEM microscopy was used to measure diameters as a function of XG/PS mixture proportion. The results presented in Table 3 suggest that there is no correlation between nanosphere average diameter

Table 3
Average measured diameter (*D*) and standard deviation (*δD*) of the measured nanospheres as a function of XG and PS proportion in mixture.

Parameter	XG/PS proportion (%)					
	(95/5)	(90/10)	(85/15)	(80/20)	(75/25)	(70/30)
$D \pm \delta D$ (nm)	No formation	567 ± 89	337 ± 71	580 ± 88	360 ± 55	334 ± 88

Measured diameter: *D* (nm) and standard deviation: *δD* (nm).

D and mixture component proportions within the range investigated.

A study was also conducted to correlate array formation with spinning speed. No array formation was observed for spinning speeds of 2000 and 3000 rpm, as shown in Fig. 5E for the XG/PS(80/20%) sample. On the other hand, the samples deposited at 1000 rpm presented a radial circular nanosphere diameter gradient, where the bigger nanospheres were positioned at the center and the smaller ones at the border, as shown in Fig. 5F. This result confirms the previous assumption made in the first section of the existence of characteristic nanosphere diameter which would be found to correspond to the balance of drag force and centrifugal force at a constant rotating speed.

4. Conclusion

Low xyloglucan content mixtures from original solutions with the same concentrations of both XG (15 mg/L) and PS (15 mg/L) components presented XG nanosphere arrays. Furthermore, XPS results for these mixtures show that equal amounts of XG and PS were adsorbed on the substrate for 50% XG as well as for 10% XG proportions. PS adsorption was not detected when the XG proportion in the mixture was 90%.

In an effort to obtain PS nanosphere arrays, the amount of the PS component in the original solution was doubled (XG (15 mg/L) and PS (30 mg/L)) to no avail. This is because the final average diameter of the PS nanospheres is still small enough to be washed away while the remaining nanospheres were buried below the XG layer. After a second increase in the PS content (XG (15 mg/L) and PS (60 mg/L)), PS nanosphere arrays were successfully fabricated on top of a homogeneous xyloglucan layer. It was also noticed that average size of the nanospheres is highly dependent on the spinning speed for the range from 400 rpm to 1100 rpm, where an inverse square-root dependence of nanosphere diameter on spinning speed was observed. The diameter was also observed to scale as the inverse of the evaporation rate but not with the mixture proportion.

Acknowledgments

The authors acknowledge the INCT for Diagnostics in Public Health, CAPES (Rede Nanobiotec) and CNPq for funding and BIOPOL/UFPR, MFA/UFPR and LITS/UFPR for material support.

References

Acrivos, A., Shah, M. J., & Peterson, E. E. (1960). On the flow of a non-Newtonian liquid on a rotating disk. *Journal of Applied Physics*, *31*(6), 963–968.

Aranberri, I., Beverley, K. J., Binks, B. P., Clint, J. H., & Fletcher, P. D. I. (2002). How do emulsions evaporate. *Langmuir*, *18*(9), 3471–3475.

Auguste, F., & Levy, F. (2009). *Emulsion science and technology*. Weinheim: Wiley-VCH., pp. 97–104.

Bhattacharyya, K. G. (1989). Adsorption of carbon dioxide on mica surfaces. *Langmuir*, *5*(5), 1155–1162.

Battacharryya, K. G. (1993). XPS study of mica surfaces. *Journal of Electron Spectroscopy and Related Phenomena*, *63*(3), 289–306.

Bhattacharya, S., Bal, S., Mukherjee, R. K., & Bhattacharya, S. (1991). Rheological behaviour of tamarind (Tamarindus indica) kernel powder (TKP) suspension. *Journal of Food Engineering*, *13*(2), 151–158.

Biresaw, G., Carriere, C. J., & Willett, J. L. (2004). Interfacial adhesion in model bioblends. *Journal of Applied Polymer Science*, *94*(1), 65–73.

Birnie, D. P., III, & Manley, M. (1997). Combined flow and evaporation of fluid on a spinning disk. *Physics of Fluids*, *9*(4), 870–875.

Bornside, D. E., Macosko, C. W., & Scriven, L. E. (1987). On the modeling of spin coating. *Journal of Imaging Technology*, *13*, 122–130.

Carroll, N. J., Pylypenko, S., Atanassov, P. B., & Petsev, D. N. (2009). Microparticles with bimodal nanoporosity derived by microemulsion templating. *Langmuir*, *25*(23), 13540–13544.

Clint, J. H., Fletcher, P. D. I., & Todorov, I. T. (1999). Evaporation rates of water from water-in-oil microemulsion. *Physical Chemistry Chemical Physics*, *1*, 5005–5009.

Cox, P. A., Egdell, R. G., Harding, C., Patterson, W. R., & Tavener, P. J. (1982). Surface properties of antimony doped tin(IV) oxide: A study by electron spectroscopy. *Surface Science*, *123*(2–3), 179–203.

Del Campo, A., & Artz, E. (2008). Fabrication approaches for generating complex micro- and nanopatterns on polymeric surfaces. *Chemical Reviews*, *108*, 911–945.

Desgouilles, S., Vauthier, C., Bazile, D., Vacus, J., Grossiord, J.-L., Veillard, M., et al. (2003). The design of nanoparticles obtained by solvent evaporation: A comprehensive study. *Langmuir*, *19*(22), 9504–9510.

Dufrêne, Y. F., Marchal, T. G., & Rouxhet, P. G. (1999). Probing the organization of adsorbed protein layers: Complementarity of atomic force microscopy, X-ray photoelectronspectroscopy and radiolabeling. *Applied Surface Science*, *144–145*, 638–643.

Emslie, A. G., Bonner, F. T., & Peck, L. G. (1958). Flow of a viscous liquid on a rotating disk. *Journal of Applied Physics*, *29*(5), 858–862.

Engel, A., Schoenenberger, A.-C., & Müller, D. J. (1997). High resolution imaging of native biological sample surfaces using scanning probe microscopy. *Current Opinion in Structural Biology*, *7*(2), 279–284.

Forrest, J. A. (2002). A decade of dynamics in thin films of polystyrene: Where are we now? *European Physical Journal E*, *8*(2), 261–266.

Friberg, S. E., & Langlois, R. C. (1992). Evaporation from emulsions. *Journal of Dispersion Science and Technology*, *13*, 223.

Fry, S. C. (1989). The structure and functions of xyloglucan. *Journal of Experimental Botany*, *40*, 1–11.

Hayashi, T. (1989). Xyloglucans on the primary cell wall. *Annual Review of Plant Physiology and Plant Molecular Biology*, *40*, 139–168.

Hulteen, J. C., & van Duyne, R. P. (1995). Nanosphere lithography: A materials general fabrication process for periodic particle array surfaces. *Journal of Vacuum Science & Technology A*, *13*, 1553–1558.

Julien, R., & Botet, R. (1987). *Aggregation and fractal aggregates*. Singapore: World Scientific Publishing Co. Pte. Ltd., pp. 77–102.

Kapilashrami, A., Eskilsson, K., Bergström, L., & Malmsten, M. (2004). Drying of oil-in-water emulsions on hydrophobic and hydrophilic substrates. *Colloid Surfaces A*, *233*(1–3), 155–161.

Kralchevsky, P. A., & Denkov, N. D. (2001). Capillary forces and structuring in layers of colloid particles. *Current Opinion in Colloid & Interface Science*, *6*(4), 383–401.

Langlois, B. R. C., & Friberg, S. E. (1993). Evaporation from a complex emulsion system. *Journal of the Society of Cosmetic Chemists*, *44*, 23–34.

Lawrence, C. (1988). The mechanics of spin coating of polymer films. *Physics of Fluids*, *31*(10), 2786–2795.

Leal-Calderon, F., Mondain-Monval, O., Pays, K., Royer, N., & Bibette, J. (1997). Water-in-oil emulsions: Role of the solvent molecular size on droplet interactions. *Langmuir*, *13*, 7008–7011.

Leung, B. O., Hitchcock, A. P., Cornelius, R., Brash, J. L., Scholl, A., & Doran, A. (2009). *Biomacromolecules*, *10*, 1838.

Liu, F.-K., Chang, Y.-C., Ko, F.-H., Chu, T.-C., & Daí, B.-T. (2003). Rapid fabrication of high quality self-assembled nanometer gold particles by spin coating method. *Microelectronic Engineering*, *67–68*, 702–709.

Liu, Z. H., & Brown, N. M. D. (1998). XPS characterization of mica surfaces processed using a radio-frequency (rf) argon plasma. *Journal of Physics D: Applied Physics*, *31*, 1771–1781.

Malmsten, M. (2003). *Biopolymers at interfaces*. New York: Marcel Dekker Inc., pp. 741–771.

Meyerhofer, D. (1978). Characteristics of resist films produced by spinning. *Journal of Applied Physics*, *49*(7), 3993–3997.

Mezzenga, R., Roukolainen, J., Fredrickson, G. H., Kramer, E. J., Moses, D., Heeger, A. J., et al. (2003). Templating organic semiconductors via self-assembly of polymer colloids. *Science*, *299*, 1872–1874.

Miyazaki, S., Suisha, F., Kawasaki, N., Shirakawa, M., Yamatoya, K., & Attwood, D. (1998). Thermally reversible xyloglucan gels as vehicles for rectal drug delivery. *Journal of Controlled Release*, *56*(1–3), 75–83.

Miyazaki, S., Kawasaki, N., Kubo, W., Endo, K., & Attwood, D. (2001). Comparison of in situ gelling formulations for the oral delivery of cimetidine. *International Journal of Pharmaceutics*, *220*(1–2), 161–168.

Norrman, K., Ghanbari-Siahkali, A., & Larsen, N. B. (2005). 6 Studies of spin-coated polymer films. *Annual Reports on the Progress. Chemistry, Section C*, *101*, 174–201.

Powell, T. B., Tran, P. L., Kim, K., & Yoon, J.-Y. (2009). Size-dependent self-assembly of sumicron/nano beads-protein conjugates for construction of a protein nanoarray. *Materials and Science Engineering C*, *29*, 2459–2463.

Reid, J. S. G. (1985). Cell wall storage carbohydrates in seeds – Biochemistry of the seed “Gums” and “Hemicelluloses”. *Advances in Botanical Research*, *11*(1), 125–155.

Russ, J. C. (1998). *The image processing handbook*. Boca Raton: CRC Press., pp. 305–333.

Tadros, T. (2009). *Emulsion science and technology*. Weinheim: Wiley–VCH., pp. 1–55.

Tormen, M., Businaro, L., Altissimo, M., Romanato, F., Cabrini, S., Perennes, F., et al. (2004). 3D patterning by means of nanoimprinting, X-ray and two-photon lithography. *Microelectronic Engineering*, *73–74*, 535–541.

Zhao, Y., & Marshall, J. S. (2008). Spin coating of a colloidal suspension. *Physics of Fluids*, *20*(4), 043302-1-15.